arXiv:1612.08841v1 [cond-mat.str-el] 28 Dec 2016

In-plane anisotropy of transport coefficients in the electronic nematic states: Universal origin of the nematicity in Fe-based superconductors

Seiichiro ONARI[1,2] and Hiroshi KONTANI[3]
[1] *Department of Physics, Okayama University, Okayama 700-8530, Japan*
[2] *Research Institute for Interdisciplinary Science, Okayama University, Okayama 700-8530, Japan*
[3] *Department of Physics, Nagoya University, Furo-cho, Nagoya 464-8602, Japan*
(Dated: December 30, 2016)

The origin of the electronic nematicity and its remarkable material-dependence are famous long-standing unsolved issues in Fe-based superconductors. To attack these issues, we focus on the in-plane anisotropy of the resistivity: In the nematic state in FeSe, the relation $\rho_x > \rho_y$ holds, where $\rho_{x(y)}$ is the resistivity along the longer (shorter) Fe-Fe axis. In contrast, the opposite anisotropy $\rho_x < \rho_y$ is realized in other undoped Fe-based superconductors. Such nontrivial material dependence is naturally explained in terms of the strongly orbital-dependent inelastic quasiparticle scattering realized in the orbital-ordered state. The opposite anisotropy between FeSe ($\rho_x > \rho_y$) and other undoped compounds ($\rho_x < \rho_y$) reflects the difference in the number of hole-pockets. We also explain the large in-plane anisotropy of the thermoelectric power in the nematic state.

PACS numbers: 74.70.Xa, 75.25.Dk, 72.10.-d, 72.15.Jf

The emergence of the electronic nematic states below the structure transition temperature $T_{\rm S}$ is one of the significant universal features in Fe-based superconductors. However, the realized electronic properties exhibit remarkable compound dependences. One example is the absence of magnetism in FeSe and the presence of magnetism in the nematic states (Néel temperature $T_{\rm N} \lesssim T_{\rm S}$) in other compounds. As possible nematic order parameters, the spin-nematic order [1, 2] and the orbital order [3–7] have been studied intensively so far. Recently, the present authors explained the nematicity without magnetization in FeSe as the orbital order caused by the Aslamazov-Larkin vertex correction [8]. The current fundamental question is whether the origin of the nematicity is universal or material-dependent [8, 9].

To answer this question, the strong in-plane anisotropy of transport coefficients has been studied intensively as a key electronic property in the nematic state [2, 10–19]. In $Ba(Fe_{1-x}Co_x)_2As_2$, $Ba(As_{1-x}P_x)_2$ and $EuFe_2(As_{1-x}P_x)_2$, large C_2 anisotropy in the resistivity $\Delta\rho \equiv \rho_x - \rho_y < 0$ appears in detwinned samples below $T_{\rm S}$, where ρ_μ is the resistivity along the μ-axis [10–12]. The relation $\Delta\rho < 0$ is observed in the non-magnetic nematic state for $T_{\rm S} > T > T_{\rm N}$, and even for $T \gtrsim T_{\rm S}$ under the weak uniaxial stress. Remarkably, the opposite anisotropy $\Delta\rho > 0$ is realized in FeSe [13, 14]. According to these observations, one may expect that the origin of nematicity in FeSe is special.

The anisotropic elastic scattering due to the impurity-induced C_2 local orbital order (orbital nematogen) [15, 16] and the magnetic nematogen [17, 18], and the anisotropic quasiparticle velocity [19] have been discussed. On the other hand, the anisotropic inelastic scattering due to the C_2 spin fluctuations was discussed based on the spin-nematic scenario [2]. In $BaFe_2As_2$ [11], the anisotropy of resistivity is reduced after the annealing, indicating that both elastic scattering and inelastic one contribute to the anisotropy in $BaFe_2As_2$. In contrast to Ba122 compounds, ρ_μ in FeSe exhibits sizable anisotropy even in the clean limit samples, in which the elastic scattering is negligible at $T \sim T_{\rm S}$ (=90K). Therefore, the in-plane resistivity anisotropy in FeSe below $T_{\rm S}$ should originate from the inelastic scattering. The opposite anisotropic relation between FeSe ($\Delta\rho > 0$) and other compounds ($\Delta\rho < 0$) provides us a crucial hint to understand the origin of the nematicity in Fe-based superconductors.

In this paper, we study the in-plane anisotropy of resistivity and thermoelectric power (TEP) below $T_{\rm S}$ based on the orbital-order scenario. Under the nematic orbital order, the spin susceptibility becomes strongly orbital-dependent, so the total spin susceptibility possesses large C_2 anisotropy: $\chi^s(\pi, 0) \gg \chi^s(0, \pi)$ [20]. Then, the inelastic scattering rate on band b, $\gamma^b_{\boldsymbol{k}}$, possesses strong in-plane anisotropy due to the orbital-dependent spin fluctuations. By taking this fact into account, the characteristic anisotropy of the transport coefficients in the nematic states are naturally understood. In particular, the anisotropy $\Delta\rho > 0$ characteristic in FeSe originates from the "singleness of the hole pocket". This study leads to the conclusion that the orbital nematicity is universal in various Fe-based superconductors.

The nematic orbital order below T_S is given by the vertex correction (VC), which represents the many-body effects beyond the random-phase-approximation (RPA) [3, 4, 8, 21]. Based on this self-consistent vertex correction (SC-VC) theory, we can explain the strong orbital fluctuations, which are measured by the softening of C_{66} and Raman study [22], and the "sign-reversing orbital polarization in $\boldsymbol{k}$-space" below $T_{\rm N}$ in FeSe [23]. This attractive orbital-order scenario is confirmed by the present study for various Fe-based superconductors.

We set the x and y axes parallel to the nearest Fe-Fe bonds, and denote the orbital $d_{3z^2-r^2}$, d_{xz}, d_{yz}, d_{xy}, and $d_{x^2-y^2}$ as $l = 1$, 2, 3, 4, and 5, respectively. We employ the eight-orbital d-p Hubbard model [8, 23] based on the first-principles calculation

$$H_{\rm M}(r) = H_{\rm M}^0 + rH_{\rm M}^U + H_{\rm M}^{\rm orb} \quad ({\rm M} = {\rm LaFeAsO, FeSe}), \quad (1)$$

where $H_{\rm M}^0$ is the eight-orbital tight-binding model, and $H_{\rm M}^U$ is the first-principles screened Coulomb potential for d-orbitals in Ref. [24]. The factor $r(< 1)$ is the parameter introduced to adjust the spin fluctuation strength. $H_{\rm M}^{\rm orb} = \sum_{\boldsymbol{k},l=2,3} \Delta E_l(\boldsymbol{k}) n_l(\boldsymbol{k})$ is given by the $\boldsymbol{k}$-dependent orbital-polarization energy $\Delta E_l(\boldsymbol{k})$ and the electron density for l orbital $n_l(\boldsymbol{k})$. $\Delta E_l(\boldsymbol{k})$ becomes 0 for $T \geq T_{\rm S}$. In the LaFeAsO model, we employ the constant orbital polarization $\Delta E_{xz}(\boldsymbol{k}) = -\Delta_E$ and $\Delta E_{yz}(\boldsymbol{k}) = \Delta_E$. In the FeSe model, we employ the sign reversing orbital polarization $\Delta E_{xz(yz)}(\boldsymbol{k})$ obtained in the previous microscopic study [23], which is consistent with angle-resolved photoemission spectroscopy (ARPES) measurements [25]. Here, the relation $\Delta E_{xz}(k_x, k_y) = -\Delta E_{yz}(k_y, k_x)$ holds, and the maximum orbital polarization is given by $\Delta_E = \Delta E_{yz}({\rm X}) = -\Delta E_{xz}({\rm Y})$. See the the Supplemental Material (SM), Sec. A [26] for details.

In the presence of $\Delta E_l(\boldsymbol{k})$, we calculate the spin (orbital) susceptibilities $\hat{\chi}^{s(c)}(q) = \hat{\chi}^{\rm irr}(q)/[1 - \hat{\Gamma}^{s(c)}\hat{\chi}^{\rm irr}(q)]^{-1}$ using the RPA, where $\chi^{\rm irr}_{ll',mm'}(q) = -\frac{T}{N}\sum_k G^0_{l,m}(k+q)G^0_{m',l'}(k)$ is the irreducible susceptibility in the orbital basis, and $\hat{\Gamma}^{s(c)}$ is the bare Coulomb interaction [27]. $\hat{G}^0$ is the Green function matrix without the self-energy. We denote $k = (\boldsymbol{k}, \epsilon_n)$ with fermion Matsubara frequency $\epsilon_n = (2n+1)\pi T$, and $q = (\boldsymbol{q}, \omega_n)$ with boson Matsubara frequency $\omega_n = 2n\pi T$. The spin Stoner factor α_s is defined as the maximum eigenvalue of $\hat{\Gamma}^s\hat{\chi}^{\rm irr}(\boldsymbol{q})$. At $T = T_{\rm N}$, $\alpha_s = 1$ is satisfied. We also calculate the self-energy matrix $\hat{\Sigma}(k) = \frac{T}{N}\sum_q \hat{V}^{\Sigma}(q)\hat{G}(k-q)$, where $\hat{G}$ is the Green function matrix, and $\hat{V}^{\Sigma}$ is the interaction matrix for the self-energy [4, 21, 23]. We employ the RPA for $\hat{V}^{\Sigma}$, and calculate $\hat{G} = [(\hat{G}^0)^{-1} - \hat{\Sigma}]^{-1}$ and $\hat{\Sigma}$ self-consistently. Details of the formulation are described in the SM, Sec. A [26]. Qualitatively similar results are obtained from the fully self-consistent approximation by including the self-energy in $\hat{V}^{\Sigma}$. Hereafter, we take $N = N_x \times N_y = 128 \times 128$ $\boldsymbol{k}$ meshes, 1024 Matsubara frequencies, and $T = 20$meV unless otherwise noted.

We start with the LaFeAsO model. Its bandstructure is similar to that of Eu122 and Ba122. Figure 1(a) shows the Fermi surfaces (FSs) for $\Delta_E = 0$, where the hole-FSs are denoted as h-FS1-3, and the electron-FSs are denoted as e-FS1,2. Figure 1(b) shows the deformed FSs for $\Delta_E = 30$meV. Here, the orbital splitting $2\Delta_E$ is comparable to the ARPES measurement in $BaFe_2As_2$ [28, 29] for $T \ll T_{\rm N}$. We put $r = 0.334$, in which the spin Stoner factor α_s is 0.898 for $\Delta_E = 0$. Then, α_s increases to 0.990 when $\Delta_E = 50$meV. Figure 1(c) shows the spin susceptibility for $\Delta_E = 30$meV, in which the relation $\chi^s_{33,33}(\pi, 0) \gg \chi^s_{22,22}(0, \pi)$ gives the prominent C_2 anisotropic spin susceptibility $\chi^s(q) \equiv \sum_{l,m}\chi^s_{ll,mm}(q)$. Such strong orbital dependence in χ^s causes the orbital-dependent quasiparticle damping $\gamma^b_{\boldsymbol{k}}(= -{\rm Im}\Sigma^b(\boldsymbol{k}, +i0))$ as shown in Fig. 1(e). The cold spot is defined as the position on the FS with minimum value of $\gamma^b_{\boldsymbol{k}}$. Since the spin fluctuations mainly develop in the d_{yz} orbital for $\Delta_E > 0$, the cold spots are located on the FS composed of the d_{xz} orbital. In Fig. 1(b), we show only the cold spots on the h-FS1,2 since they are significant for the C_2 transport phenomena. The anisotropy in the transport coefficients is determined by the positions of the cold spots. Note that, in the present study, we ignore the damping due to the orbital fluctuations caused by the VC. However, the positions of cold spots are unchanged by the orbital fluctuations since only $\chi^c_{33,33}$ is enhanced by the VC [30]. Therefore, the anisotropy in the transport coefficients obtained in this study is expected to be unchanged. This is our important future issue.

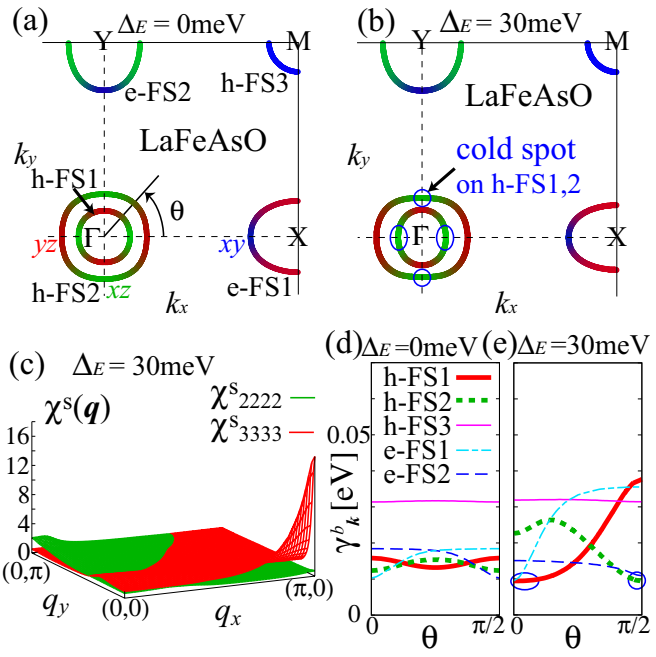

FIG. 1: (a) The hole-like FSs (h-FS1-3) and the electron-like FSs (e-FS1,2) in the LaFeAsO model for $\Delta_E = 0$ and (b) those for $\Delta_E = 30$meV, where θ denotes the azimuthal angle on a FS ($\theta = 0$ corresponds to the k_x direction). The colors correspond to 2 (green), 3 (red), and 4 (blue), respectively. (c) $\boldsymbol{q}$ dependencies of $\chi^s_{22,22}(\boldsymbol{q})$ and $\chi^s_{33,33}(\boldsymbol{q})$ for $\Delta_E = 30$meV ($\alpha_s = 0.967$). (d) θ dependences of $\gamma^b_{\boldsymbol{k}}$ on the FSs for $\Delta_E = 0$ and (e) those for $\Delta_E = 30$meV. Cold spots on the h-FS1,2 are marked by blue circles in (b) and (e).

Next, we move to the FeSe model. We introduce the mass enhancement factor $z_{xy}^{-1} = 1.6$ by following

Refs. [8, 23]. In Figs. 2(a) and 2(b), the FSs for $\Delta_E = 0$meV and the FSs for $\Delta_E = 30$meV are shown, respectively. The h-FS1 and h-FS3 are absent in the present FeSe model [31]. We put $r = 0.218$, where α_s is 0.846 for $\Delta_E = 0$meV. Then, α_s increases to 0.870 when $\Delta_E = 50$meV. As shown in Fig. 2(c), the spin susceptibilities for $\Delta_E = 30$meV have the orbital-dependent C_2 anisotropy $\chi^s_{33,33}(\pi, 0) > \chi^s_{22,22}(0, \pi)$. Figures 2(d) and 2(e) show the momentum dependences of $\gamma^b_{\boldsymbol{k}}$ on the FSs for $\Delta_E = 0$meV and those for $\Delta_E = 30$meV, respectively. In Figs. 2(b) and 2(e), we show the cold spots on the h-FS2, which play an important role for the C_2 transport phenomena.

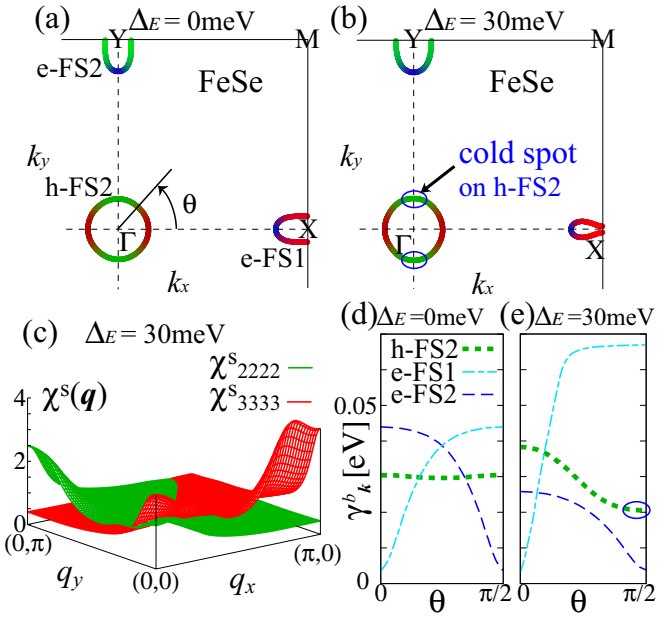

FIG. 2: (a) FSs of the FeSe model for $\Delta_E = 0$ and (b) those for $\Delta_E = 30$meV. Here, the h-FS1 and h-FS3 are absent. (c) $\boldsymbol{q}$ dependencies of $\chi^s_{22,22}(\boldsymbol{q})$ and $\chi^s_{33,33}(\boldsymbol{q})$ for $\Delta_E = 30$meV ($\alpha_s = 0.867$). (d) θ dependences of $\gamma^b_{\boldsymbol{k}}$ on the FSs for $\Delta_E = 0$ and (e) those for $\Delta_E = 30$meV. The cold spots on the h-FS2 are marked by blue circles.

Next, we study the resistivity ρ due to the strongly anisotropic inelastic scattering. Using the linear response theory, the conductivity σ_μ along the $\mu(= x, y)$ direction is obtained by

$$\sigma_\mu = \frac{e^2}{N} \sum_{\boldsymbol{k},b} \int_{-\infty}^{\infty} \frac{d\omega}{\pi} \left(-\frac{\partial f(\omega)}{\partial \omega} \right) \left| v^\mu_{b,\boldsymbol{k}} G^b_{\boldsymbol{k}}(\omega + i0) \right|^2, \quad (2)$$

where $-e$ is the charge of an electron, and $f(\omega)$ is the Fermi distribution function. $v^\mu_{b,\boldsymbol{k}} = \frac{\partial \varepsilon^b_{\boldsymbol{k}}}{\partial k_\mu}$ is the velocity along the μ direction, where $\varepsilon^b_{\boldsymbol{k}}$ is the dispersion of band b. $G^b_{\boldsymbol{k}}(\omega + i0)$ denotes the retarded Green function. In this study, we neglect the VC for the current, since its effect is small for ρ and the TEP [32–35], whereas it is important for the Hall coefficient and magnetoresistance [32–35]. The study of the current VC is our important future issue.

Figure 3(a) shows the resistivity $\rho_\mu = 1/\sigma_\mu$ obtained for $\Delta E_{xz} = -50$-0meV in the LaFeAsO model at $T = 20$meV. We also show the T dependence of ρ_μ in the LaFeAsO model in Fig. 3(b) by assuming the T dependence of Δ_E as the mean-field-like behavior $\Delta_E = \Delta^0_E \tanh(1.74\sqrt{T_S/T - 1})$. Here, we put $\Delta^0_E = 50$meV and $T_S = 20$meV. Then, we obtain $T_N = 16$meV from the condition $\alpha_s = 1$. The obtained in-plane anisotropy $\Delta\rho < 0$ below T_S is consistent with the experimental results in Ba122 [10, 11] and Eu122 [12]. In contrast, in Figs. 3(c) and 3(d), the opposite in-plane anisotropy $\Delta\rho > 0$ is obtained in the FeSe model. This result is also consistent with the experiments in FeSe [13, 14].

Here, we explain why the obtained in-plane anisotropy of resistivity is opposite between the FeSe model and the LaFeAsO model. In both systems, the anisotropy of ρ mainly stems from the hole-pockets h-FS1,2, of which the schematic figures are shown in Fig. 3(e). Since the Fermi velocity on the cold spots on the h-FS1 (h-FS2) is parallel to k_x-axis (k_y-axis), the h-FS1 (h-FS2) contributes to the relation $\Delta\rho < 0$ ($\Delta\rho > 0$). In the LaFeAsO model, the relation $\Delta\rho < 0$ is realized since the area of the cold spot on the h-FS1 around $\theta \sim 0$ is very wide as shown in Figs. 1(b) and 1(e). In contrast, in the FeSe model, the opposite relation $\Delta\rho > 0$ is realized by the cold spots on the h-FS2 since the h-FS1 is absent.

We verified that the e-FSs are not essential for the opposite anisotropy of resistivity between FeSe and LaFeAsO. In both models, the cold spots on the e-FSs are located on the d_{xy} orbital region, and the area of the cold spot on the e-FS1 is narrower than that on the e-FS2 in the orbital-ordered state due to the strong spin fluctuations on the d_{yz} orbital: See Figs. 1(e) and 2(e). For this reason, the e-FSs contribute to the relation $\Delta\rho \gtrsim 0$ below T_S. In FeSe, both the h-FSs and the e-FSs contribute to the positive $\Delta\rho$. In LaFeAsO, $\Delta\rho$ is negative since the contribution from the e-FSs are considerably small. Therefore, we conclude that the opposite in-plane anisotropy of resistivity between FeSe and LaFeAsO originates from the presence or absence of the inner hole-pocket.

In Fig. 3(f), we also show the carrier doping (δn) dependences of the in-plane anisotropy of ρ in the LaFeAsO model for $\Delta_E = 50$meV. For each δn, r is adjusted to satisfy $\alpha_s = 0.990$ for $\Delta_E = 50$meV. In heavily hole-doped case ($\delta n < -0.12$), $\Delta\rho$ is reversed to positive since the contribution from the h-FS2 becomes large, consistently with previous theoretical and experimental reports [2, 36–38]. Details are described in the SM, Sec. C [26].

The anisotropy $\rho_x \neq \rho_y$ due to the C_2 spin fluctuations has been discussed in terms of the spin-nematic scenario [2, 36]. In the present paper, we explained that the orbital dependence of the spin fluctuations, which is ignored in the spin-nematic theory, is essential to un-

derstand the characteristic difference between FeSe and Ba122. In FeSe, the anisotropy of ρ should originate from the inelastic scattering since the sample is very clean. In Ba122, in contrast, the anisotropic elastic scattering (nematogen) also gives sizable contribution as discussed in Refs. [15–19].

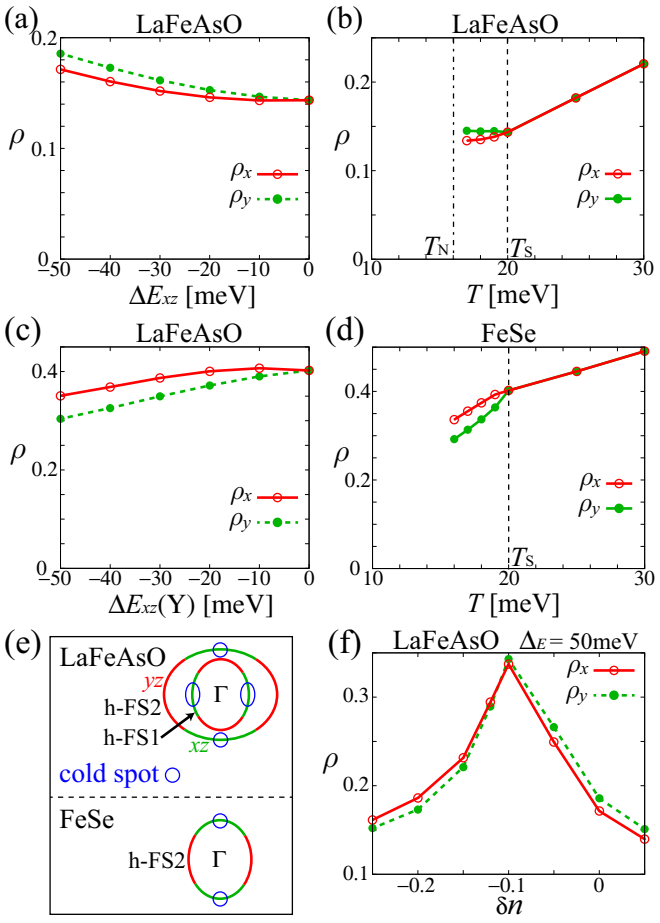

FIG. 3: (a) ΔE_{xz} dependence of ρ_μ, and (b) T dependence of ρ_μ in the LaFeAsO model. (c) ΔE_{xz}(Y) dependence of ρ_μ, and (d) T dependence of ρ_μ in the FeSe model. $\rho = 1$ corresponds to $(\hbar a_c)/e^2 \sim 250\mu$cm$\Omega$ for the interlayer distance $a_c = 0.6$nm. (e) Schematic figures of FSs with the cold spots around the Γ point. (f) Carrier doping δn dependence of ρ_μ for $\alpha_s = 0.990$ and $\Delta_E = 50$meV in the LaFeAsO model.

Here, we briefly analyze the TEP S, which is given as $S_\mu = \frac{1}{\sigma_\mu}\sum_b \alpha^b_\mu$, where

$$\alpha^b_\mu = -\frac{e}{TN}\sum_{\boldsymbol{k}}\int_{-\infty}^{\infty}\frac{d\omega}{\pi}\left(-\frac{\partial f(\omega)}{\partial\omega}\right)\omega\left|v^\mu_{b,\boldsymbol{k}}G^b_{\boldsymbol{k}}(\omega+i0)\right|^2 \quad (3)$$

is the Peltier conductivity on band b. Figure 4(a) shows the C_2 anisotropy of the TEP induced by the orbital polarization in the LaFeAsO model. Here, $\tilde{S}_\mu$ is defined as $\tilde{S}_\mu \equiv S_\mu - S^0$, where S^0 is the TEP at $\Delta_E = 0$meV. The value of $\tilde{S}_y$ remarkably increases with the orbital polarization, which is consistent with the experimental results in Eu122 [12]. This result is mainly caused by the strong energy dependence of $\gamma^b_{\boldsymbol{k}}$ near the cold spots on the h-FS2: See the SM, Sec. B [26] for details. We note that S^0 is sensitive to details of the model, because of the large cancellation between positive α^b from the h-FSs and negative α^b from the e-FSs. In fact, $S^0 \sim -10\mu$V/K in the present d-p model, whereas $S^0 \sim 0$meV in the five d-orbital LaFeAsO model analyzed in Ref. [4]. Nonetheless, the relations $\tilde{S}_y > 0$ and $\tilde{S}_x < 0$ in Fig. 4(a) are robust and model-independent. In Fig. 4(b), we show the δn dependence of $\tilde{S}_\mu$ in the LaFeAsO model for $\Delta_E = 50$meV by adjusting r to satisfy $\alpha_s = 0.990$. The anisotropy of S is reversed in heavily hole-doped case ($\delta n < -0.15$).

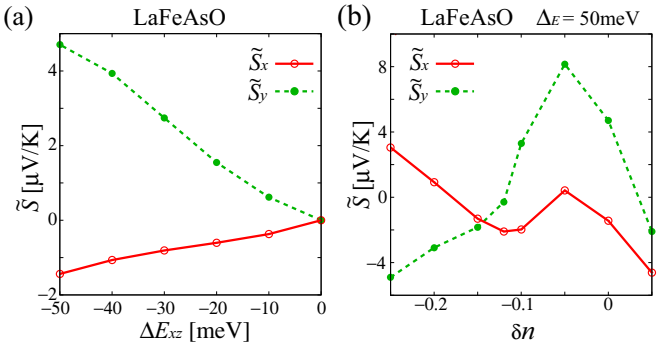

FIG. 4: (a) ΔE_{xz} dependence of $\tilde{S}_\mu \equiv S_\mu - S^0$ in the LaFeAsO model, and (b) carrier doping δn dependence of $\tilde{S}_\mu$ for $\alpha_s = 0.990$ and $\Delta_E = 50$meV in the LaFeAsO model.

In the SM, Sec. D [26], we also study the LaFeAsO model with the orbital polarization only on the e-FSs, which is suggested by the ARPES measurement in Ba122 [28]. The obtained anisotropies of ρ and S are qualitatively the same as the case of all FSs are polarized, since the structures of C_2 spin fluctuations and $\gamma^b_{\boldsymbol{k}}$ are essentially unchanged. In the SM, Sec. E [26], we study the effect of the spin-orbit interaction (SOI) [39] on the transport properties in FeSe.

Finally, we stress that the TEP is magnified by the mass-enhancement factor z^{-1} as shown in Eq. (S5) in the SM, Sec. B [26]. The value of z^{-1} observed by experiments is $z^{-1} \sim$ 3-5 in $EuFe_2As_2$ [40] and $BaFe_2As_2$ [41–43]. Using the experimental z^{-1}, we can understand $S_y - S_x \sim 20\mu$V/K observed in Eu122 near T_N [12].

In summary, we studied the anisotropy in the transport coefficients in the nematic states to clarify the true nematic order parameter in Fe-based superconductors [8, 9]. Once the orbital order sets in, the inelastic scattering rate $\gamma^b_{\boldsymbol{k}}$ becomes very anisotropic due to the prominent orbital-dependent spin fluctuations. For this reason, the characteristic material-dependent C_2 transport phenomena below T_S are naturally explained based on the realistic multiorbital Hubbard models. In particular, the opposite anisotropy $\rho_x > \rho_y$ in FeSe originates from the

singleness of the hole pocket. In addition, the thermoelectric power shows sizable in-plane anisotropy due to the strong energy-dependence of $\gamma^b_{\boldsymbol{k}}$. This study leads to the conclusion that the orbital order scenario, which is microscopically supported by the SC-VC theory, is universal in various Fe-based superconductors.

We are grateful to Y. Yamakawa and T. Fujii for valuable discussions. This work was supported by JSPS KAKENHI Grant Number JP26800185. Part of numerical calculations was performed on the Yukawa Institute Computer Facility.

[1] R. M. Fernandes, L. H. VanBebber, S. Bhattacharya, P. Chandra, V. Keppens, D. Mandrus, M. A. McGuire, B. C. Sales, A. S. Sefat, and J. Schmalian, Phys. Rev. Lett. **105**, 157003 (2010).
[2] R. M. Fernandes, E. Abrahams, and J. Schmalian, Phys. Rev. Lett. **107**, 217002 (2011).
[3] S. Onari and H. Kontani, Phys. Rev. Lett. **109**, 137001 (2012).
[4] S. Onari, Y. Yamakawa, and H. Kontani, Phys. Rev. Lett. **112**, 187001 (2014).
[5] F. Krüger, S. Kumar, J. Zaanen, and J. van den Brink, Phys. Rev. B **79**, 054504 (2009).
[6] W. Lv, J. Wu, and P. Phillips, Phys. Rev. B **80**, 224506 (2009).
[7] C.-C. Lee, W.-G. Yin, and W. Ku, Phys. Rev. Lett. **103**, 267001 (2009).
[8] Y. Yamakawa, S. Onari and H. Kontani, Phys. Rev. X **6**, 021032 (2016).
[9] A. V. Chubukov, M. Khodas, and R. M. Fernandes, Phys. Rev. X **6**, 041045 (2016).
[10] J-H. Chu, J. G. Analytis, K. D. Greve, P. L. McMahon, Z. Islam, Y. Yamamoto, and I. R. Fisher, Science **329**, 824 (2010).
[11] S. Ishida, M. Nakajima, T. Liang, K. Kihou, C. H. Lee, A. Iyo, H. Eisaki, T. Kakeshita, Y. Tomioka, T. Ito, and S. Uchida, J. Am. Chem. Soc. **135**, 3158 (2013).
[12] S. Jiang, H. S. Jeevan, J. Dong, and P. Gegenwart, Phys. Rev. Lett. **110**, 067001 (2013).
[13] M. D. Watson, T. K. Kim, A. A. Haghighirad, N. R. Davies, A. McCollam, A. Narayanan, S. F. Blake, Y. L. Chen, S. Ghannadzadeh, A. J. Schofield, M. Hoesch, C. Meingast, T. Wolf, and A. I. Coldea, Phys. Rev. B **91**, 155106 (2015)
[14] M. A. Tanatar, A. E. Böhmer, E. I. Timmons, M. Schütt, G. Drachuck, V. Taufour, K. Kothapalli, A. Kreyssig, S. L. Bud'ko, P. C. Canfield, R. M. Fernandes, and R. Prozorov, Phys. Rev. Lett. **117**, 127001 (2016).
[15] C.-C. Chen, J. Maciejko, A. P. Sorini, B. Moritz, R. R. P. Singh, and T. P. Devereaux, Phys. Rev. B **82**, 100504(R) (2010).
[16] Y. Inoue, Y. Yamakawa, and H. Kontani, Phys. Rev. B **85**, 224506 (2012).
[17] T.-M. Chuang, M. P. Allan, J. Lee, Y. Xie, N. Ni, S. L. Bud'ko, G. S. Boebinger, P. C. Canfield, and J. C. Davis, Science **327**, 181 (2010).
[18] M. N. Gastiasoro, P. J. Hirschfeld, and B. M. Andersen, Phys. Rev. B **89**, 100502(R) (2014)
[19] K. Sugimoto, P. Prelovšek, E. Kaneshita, and T. Tohyama, Phys. Rev. B **90**, 125157 (2014).
[20] H. Kontani, T. Saito, and S. Onari, Phys. Rev. B **84**, 024528 (2011).
[21] S. Onari and H. Kontani, (ed. P.D. Johnson, G. Xu, and W.-G. Yin, Springer Verlag Berlin and Heidelberg GmbH & Co. K (2015)).
[22] H. Kontani and Y. Yamakawa, Phys. Rev. Lett. **113**, 047001 (2014).
[23] S. Onari, Y. Yamakawa, and H. Kontani, Phys. Rev. Lett. **116**, 227001 (2016).
[24] T. Miyake, K. Nakamura, R. Arita, and M. Imada, J. Phys. Soc. Jpn. **79**, 044705 (2010).
[25] Y. Suzuki, T. Shimojima, T. Sonobe, A. Nakamura, M. Sakano, H. Tsuji, J. Omachi, K. Yoshioka, M. Kuwata-Gonokami, T. Watashige, R. Kobayashi, S. Kasahara, T. Shibauchi, Y. Matsuda, Y. Yamakawa, H. Kontani, and K. Ishizaka, Phys. Rev. B **92**, 205117 (2015).
[26] See Supplemental Material at .
[27] H. Kontani and S. Onari, Phys. Rev. Lett. **104**, 157001 (2010).
[28] M. Yi, D. Lu, J.-H. Chu, J. G. Analytis, A. P. Sorini, A. F. Kemper, B. Moritz, S.-K. Mo, R. G. Moore, M. Hashimoto, W.-S. Lee, Z. Hussain, T. P. Devereaux, I. R. Fisher, and Z.-X. Shen, Proc. Natl. Acad. Sci. U.S.A. **108**, 6878 (2011).
[29] T. Shimojima, T. Sonobe, W. Malaeb, K. Shinada, A. Chainani, S. Shin, T. Yoshida, S. Ideta, A. Fujimori, H. Kumigashira, K. Ono, Y. Nakashima, H. Anzai, M. Arita, A. Ino, H. Namatame, M. Taniguchi, M. Nakajima, S. Uchida, Y. Tomioka, T. Ito, K. Kihou, C. H. Lee, A. Iyo, H. Eisaki, K. Ohgushi, S. Kasahara, T. Terashima, H. Ikeda, T. Shibauchi, Y. Matsuda, and K. Ishizaka, Phys. Rev. B **89**, 045101 (2014).
[30] Y. Yamakawa and H. Kontani, arXiv:1609.09618.
[31] In the present FeSe model, we shift $E_4(\boldsymbol{k})$ around the Γ point by -0.6eV in the original FeSe model in Ref. [8] in order to realize the single hole-pocket.
[32] H. Kontani, K. Kanki, and K. Ueda, Phys. Rev. B **59**, 14723 (1999).
[33] H. Kontani, J. Phys. Soc. Jpn. **70**, 2840 (2001).
[34] H. Kontani, Rep. Prog. Phys. **71**, 026501 (2008).
[35] L. Fanfarillo, E. Cappelluti, C. Castellani, and L. Benfatto, Phys. Rev. Lett. **109**, 096402 (2012).
[36] M. Breitkreiz, P. M. R. Brydon, and C. Timm, Phys. Rev. B **90**, 121104(R) (2014).
[37] J. J. Ying, X. F. Wang, T. Wu, Z. J. Xiang, R. H. Liu, Y. J. Yan, A. F. Wang, M. Zhang, G. J. Ye, P. Cheng, J. P. Hu, and X. H. Chen, Phys. Rev. Lett. **107**, 067001 (2011).
[38] E. C. Blomberg, M. A. Tanatar, R. M. Fernandes, I. I. Mazin, Bing Shen, Hai-Hu Wen, M. D. Johannes, J. Schmalian, and R. Prozorov, Nat. Commun. **4**, 1914 (2013).
[39] T. Saito, Y. Yamakawa, S. Onari, and H. Kontani, Phys. Rev. B **92**, 134522 (2015).
[40] P. F. S. Rosa, B. Zeng, C. Adriano, T. M. Garitezi, T. Grant, Z. Fisk, L. Balicas, M. D. Johannes, R. R. Urbano, and P. G. Pagliuso, Phys. Rev. B **90**, 195146 (2014).
[41] P. Walmsley, C. Putzke, L. Malone, I. Guillamón, D. Vignolles, C. Proust, S. Badoux, A. I. Coldea, M. D. Watson, S. Kasahara, Y. Mizukami, T. Shibauchi, Y. Matsuda, and A. Carrington, Phys. Rev. Lett. **110**, 257002 (2013).
[42] K. Hashimoto, K. Cho, T. Shibauchi, S. Kasahara, Y.

Mizukami, R. Katsumata, Y. Tsuruhara, T. Terashima, H. Ikeda, M. A. Tanatar, H. Kitano, N. Salovich, R. W. Giannetta, P. Walmsley, A. Carrington, R. Prozorov, and Y. Matsuda, Science **336**, 1554 (2012).

[43] Z. Diao, D. Campanini, L. Fang, W. K. Kwok, U. Welp, and A. Rydh, Phys. Rev. B **93**, 014509 (2016).

[Supplementary Material]
In-plane anisotropy of transport coefficients in the electronic nematic states: Universal origin of the nematicity in Fe-based superconductors

Seiichiro Onari[1,2] and Hiroshi Kontani[3]

[1] *Department of Physics, Okayama University, Okayama 700-8530, Japan*
[2] *Research Institute for Interdisciplinary Science, Okayama University, Okayama 700-8530, Japan*
[3] *Department of Physics, Nagoya University, Nagoya 464-8602, Japan*

A: Details of the eight-orbital models and formulation

Here, we introduce the eight-orbital d-p models $H^0_{\rm M}$ (M=FeSe, LaFeAsO) analyzed in the main text. We first derived the first-principles tight-binding models using the WIEN2k and WANNIER90 codes. For FeSe, in order to obtain the experimentally observed Fermi surfaces (FSs), we introduce the $\boldsymbol{k}$-dependent shifts for orbital l, $\delta E_l(\boldsymbol{k})$, by introducing the intra-orbital hopping parameters as explained in Ref. [8]. We shift the d_{xy}-orbital band [$d_{xz/yz}$-orbital band] at (Γ, M, X) points by (−0.60, −0.25, +0.24) [(−0.24, 0, +0.12)], in unit eV. In Figs. S1(a) and S1(b), we show the obtained band dispersions for the LaFeAsO model and the FeSe model, respectively.

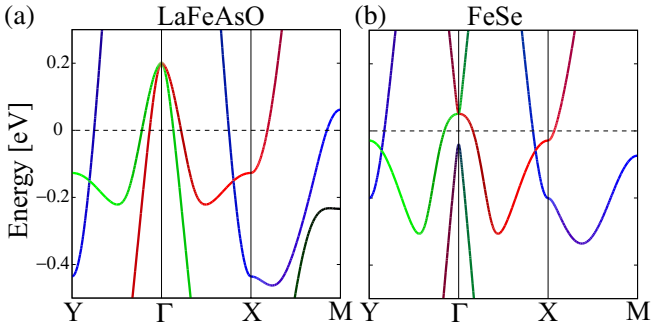

FIG. S1: Band dispersions for (a) the LaFeAsO model and (b) the FeSe model. The colors correspond to 2 (green), 3 (red), and 4 (blue), respectively.

Next, we explain the orbital polarization term $H^{\rm orb}_{\rm M}$. For the FeSe model used in the main text is given by the symmetry-breaking self-energy method developed in previous paper [23]. The obtained sign-reversing orbital polarization is shown in Fig. S2. In this orbital polarization, the relation $\Delta E_{xz}(\Gamma) - \Delta E_{yz}(\Gamma) > 0$ and $\Delta E_{xz}(\mathrm{Y}) - \Delta E_{yz}(\mathrm{X}) < 0$ holds, consistently with the ARPES measurements [25].

Finally, we explain the multiorbital Coulomb interaction $H^U_{\rm M}$. The bare Coulomb interaction for the spin

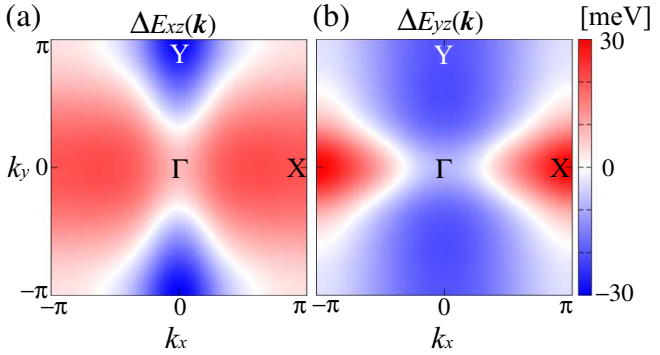

FIG. S2: $\boldsymbol{k}$-dependences of the orbital polarization (a) $\Delta E_{xz}(\boldsymbol{k})$ and (b) $\Delta E_{yz}(\boldsymbol{k})$ for $\Delta_E = 30$meV obtained by the symmetry-breaking self-energy method in the FeSe model [23].

channel is given as

$$(\Gamma^{\rm s})_{l_1l_2,l_3l_4} = \begin{cases} U_{l_1,l_1}, & l_1=l_2=l_3=l_4 \\ U'_{l_1,l_2}, & l_1=l_3\neq l_2=l_4 \\ J_{l_1,l_3}, & l_1=l_2\neq l_3=l_4 \\ J_{l_1,l_2}, & l_1=l_4\neq l_2=l_3 \\ 0, & \text{otherwise.} \end{cases} \quad \text{(S1)}$$

Also, the bare Coulomb interaction for the charge channel is

$$(\hat{\Gamma}^{\rm c})_{l_1l_2,l_3l_4} = \begin{cases} -U_{l_1,l_1}, & l_1=l_2=l_3=l_4 \\ U'_{l_1,l_2}-2J_{1_1,l_2}, & l_1=l_3\neq l_2=l_4 \\ -2U'_{l_1,l_3}+J_{l_1,l_3}, & l_1=l_2\neq l_3=l_4 \\ -J_{1_1,l_2}, & l_1=l_4\neq l_2=l_3 \\ 0. & \text{otherwise.} \end{cases} \quad \text{(S2)}$$

Here, $U_{l,l}$, $U'_{l,l'}$ and $J_{l,l'}$ are the first-principles Coulomb interaction terms given in Ref. [24]. The interaction matrix for the self-energy $\hat{V}^{\Sigma}$ is given as [4, 21, 23]

$$\begin{aligned} \hat{V}^{\Sigma}(q) \;=\; & \frac{3}{2}\hat{\Gamma}^s\hat{\chi}^s(q)\hat{\Gamma}^s + \frac{1}{2}\hat{\Gamma}^c\hat{\chi}^c(q)\hat{\Gamma}^c \\ & -\frac{1}{4}(\hat{\Gamma}^c-\hat{\Gamma}^s)\hat{\chi}^{\rm irr}(q)(\hat{\Gamma}^c-\hat{\Gamma}^s) \\ & -\frac{1}{8}(\hat{\Gamma}^c+\hat{\Gamma}^s)\hat{\chi}^{\rm irr}(q)(\hat{\Gamma}^c+\hat{\Gamma}^s). \end{aligned} \quad \text{(S3)}$$

B: Origin of the large in-plane anisotropy of S in the LaFeAsO model

In the following, we explain the reason why the in-plane anisotropy of S becomes large with increasing Δ_E in the LaFeAsO model. α_μ^b introduced in Eq. (3) in the main text is rewritten as

$$\alpha_\mu^b = -\frac{e}{T}\int_{\rm FS}\frac{dk_\parallel^b}{(2\pi)^2}\int\frac{d\epsilon_{\boldsymbol{k}}^{b*}}{|v_{b,\boldsymbol{k}}|}\left(-\frac{\partial f}{\partial\epsilon}\right)_{\epsilon=\epsilon_{\boldsymbol{k}}^{b*}}\frac{\epsilon_{\boldsymbol{k}}^{b*}|v_{b,\boldsymbol{k}}^\mu|^2}{\gamma_{\boldsymbol{k}}^b} \quad \text{(S4)}$$

$$\approx -\frac{e\pi^2T}{3}\int_{\rm FS}\frac{dk_\parallel^b}{(2\pi)^2}\frac{1}{z_{\boldsymbol{k}}^b|v_{b,\boldsymbol{k}}|}\frac{\partial}{\partial k_\perp^b}\left(\frac{|v_{b,\boldsymbol{k}}^\mu|^2}{|v_{b,\boldsymbol{k}}|\gamma_{\boldsymbol{k}}^b}\right), \quad \text{(S5)}$$

where $k_\parallel^b$ and $k_\perp^b$ denote $\boldsymbol{k}$ along the FS and $\boldsymbol{k}$ perpendicular to the FS on band b, respectively. $\epsilon_{\boldsymbol{k}}^{b*}$ is the renormalized quasiparticle energy given by $\epsilon_{\boldsymbol{k}}^{b*} = z_{\boldsymbol{k}}^b[\varepsilon_{\boldsymbol{k}}^b + {\rm Re}\Sigma^b(\boldsymbol{k},0+i0)-\mu]$, and $\gamma_{\boldsymbol{k}}^b = -{\rm Im}\Sigma^b(\boldsymbol{k},\epsilon_{\boldsymbol{k}}^{b*}+i0)$ is the quasiparticle damping without renormalization. The mass renormalization factor $z_{\boldsymbol{k}}^b$ is given by $z_{\boldsymbol{k}}^b = \left[1-\frac{\partial{\rm Re}\Sigma^b(\boldsymbol{k},\omega+i0)}{\partial\omega}|_{\omega=0}\right]^{-1}$. According to Eq. (S4), α_μ^b is sensitively influenced by the $\epsilon_{\boldsymbol{k}}^{b*}$ dependence of $1/\gamma_{\boldsymbol{k}}^b$, and $1/\gamma_{\boldsymbol{k}}^b$ is strongly energy-dependent in correlated electron systems. For instance, $\alpha_\mu^b \sim 0$ is obtained when $1/\gamma_{\boldsymbol{k}}^b$ is symmetric with respect to $\epsilon_{\boldsymbol{k}}^{b*} \to -\epsilon_{\boldsymbol{k}}^{b*}$ since $\epsilon_{\boldsymbol{k}}^{b*}\left(-\frac{\partial f}{\partial\epsilon}\right)_{\epsilon=\epsilon_{\boldsymbol{k}}^{b*}}$ is an odd function of $\epsilon_{\boldsymbol{k}}^{b*}$.

Here, we introduce $\alpha_\mu^b(\boldsymbol{k})$ as

$$\alpha_\mu^b(\boldsymbol{k}) = -\frac{e}{T}\int_{-\infty}^{\infty}\frac{d\omega}{\pi}\left(-\frac{\partial f(\omega)}{\partial\omega}\right)\omega\left|v_{b,\boldsymbol{k}}^\mu G_{\boldsymbol{k}}^b(\omega+i0)\right|^2. \quad \text{(S6)}$$

Then, the Peltier conductivity for band b is $\alpha_\mu^b = \frac{1}{N}\sum_{\boldsymbol{k}}\alpha_\mu^b(\boldsymbol{k})$. In Fig. S3(a), we show the obtained $\boldsymbol{k}$ dependence of $\alpha_y^{b=2}(\boldsymbol{k})$ on band2 including the h-FS2 around the Γ point in the LaFeAsO model for $\Delta_E = 50$meV. $\alpha_y^{b=2}(\boldsymbol{k})$ has large value around the cold spots, and the area for positive $\alpha_y^{b=2}(\boldsymbol{k})$ is much wider than the area for negative $\alpha_y^{b=2}(\boldsymbol{k})$. This result originates from the highly asymmetric $\boldsymbol{k}$ dependence of $1/\gamma_{\boldsymbol{k}}^{b=2}$ near the Fermi momentum. In Fig. S3(b), we show $\epsilon_{\boldsymbol{k}}^{b*}$ for $b=1$ (h-FS1) and $b=2$ (h-FS2) in the upper panel, and $1/\gamma_{\boldsymbol{k}}^{b=2}$ and $\alpha_y^{b=2}(\boldsymbol{k})$ on the band2 in the lower panel, as functions of $\boldsymbol{k}$ along the green arrow illustrated in Fig. S3(a). We see that the positive value of $\alpha_y^{b=2}(\boldsymbol{k})$ is much larger than the negative value of $\alpha_y^{b=2}(\boldsymbol{k})$ in magnitude. In addition, both $\alpha_y^{b=2}(\boldsymbol{k})$ and $1/\gamma_{\boldsymbol{k}}^{b=2}$ take the maxima at $\boldsymbol{k}=\boldsymbol{k}^*$. Thus, the large positive $\tilde{S}_y$ originates from the strong asymmetry of $1/\gamma_{\boldsymbol{k}}^b$ near the Fermi surface [33]. The asymmetry of $1/\gamma_{\boldsymbol{k}}^b$ is caused by the orbital dependence of $\gamma_{\boldsymbol{k}}^b$. In the orbital basis, we explain in the main text that the quasiparticle damping for the d_{yz} orbital is much larger than that for the d_{xz} orbital ($\gamma_{yz} \gg \gamma_{xz}$) since the spin fluctuations develop mainly on the d_{yz} orbital. As shown by the colors on the band dispersion in Fig. S3(b), d_{xz} orbital is dominant for $\boldsymbol{k} \approx \boldsymbol{k}^*$, and weight of d_{yz} orbital increases as $\boldsymbol{k}$ approaches to the Γ point. Thus, the asymmetric energy dependence of $1/\gamma_{\boldsymbol{k}}^b$ stems from the suppression by γ_{yz}. On the other hand, S_x slightly decreases with increasing Δ_E mainly due to the contribution from the cold spots on the e-FSs.

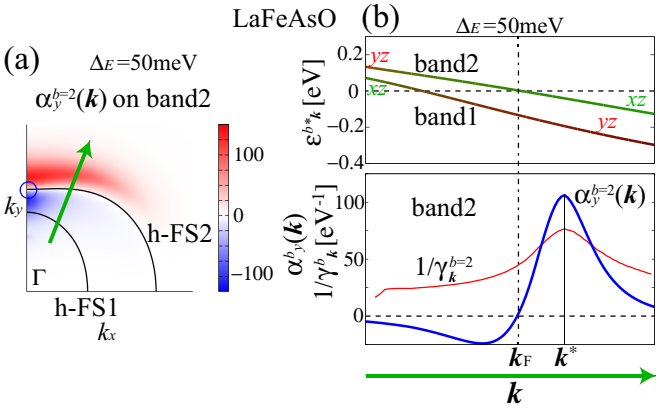

FIG. S3: (a) $\boldsymbol{k}$ dependence of $\alpha_y^{b=2}(\boldsymbol{k})$ around h-FS2 in the LaFeAsO model for $\Delta_E = 50$meV. (b) $\boldsymbol{k}$ dependences of $\epsilon_{\boldsymbol{k}}^{b*}$ for $b=1$ and 2 in the upper panel, $\alpha_y^{b=2}(\boldsymbol{k})$ and $1/\gamma_{\boldsymbol{k}}^{b=2}$ in the lower panel, as functions of $\boldsymbol{k}$ along the green arrow in (a).

C: Carrier doping dependence of the in-plane anisotropies in ρ and S in the LaFeAsO model

Here, we study the carrier doping δn dependence of the in-plane anisotropies in ρ and S. In the hole-doped compounds $Ba_{1-x}K_xFe_2As_2$, ρ_x is slightly larger than ρ_y [37, 38], which is opposite to the relation $\Delta\rho < 0$ observed in the non-doped and the electron-doped Ba122. In Fig. 3(f) in the main text, we show the δn dependence of ρ_μ for $\Delta_E = 50$meV in the LaFeAsO model. α_s is set as 0.990. The obtained sign reversal in the hole-doped region ($\delta n < -0.12$) is consistent with experimental results in the hole-doped $Ba_{1-x}K_xFe_2As_2$ [37, 38]. In the hole-doped LaFeAsO model, the FSs and the cold spots are shown in Fig. S4(a). The relation $\Delta\rho > 0$ is mainly originates from the h-FS2, since the anisotropy of γ on the h-FS2 is larger than that on the h-FS1 as shown in Fig. S4(b).

In Fig. 4(b) in the main text, we also show the δn dependences of $\tilde{S}_\mu$ for $\Delta_E = 50$meV in the LaFeAsO model. α_s is set as 0.990. We obtain the reverse of the in-plane anisotropy ($S_x > S_y$) in heavily hole-doped case ($\delta n < -0.15$). This reversal is caused by the competition between the contribution from the h-FS1 and that from the h-FS2: The h-FS1 contributes to the relation $S_x > S_y$, while the h-FS2 contributes to the opposite relation $S_x < S_y$. The former contribution becomes larger than the latter contribution in hole-doped case ($\delta n < -0.15$). We note that the contribution from

the e-FSs is unimportant for the anisotropies of ρ and S, since the area of cold spot on the e-FS1 is very narrow and $\gamma^b_{\boldsymbol{k}}$ on the e-FS2 is almost isotropic as shown in Fig. S4(b).

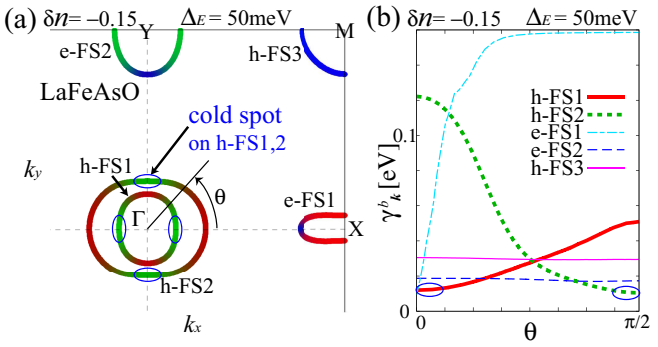

FIG. S4: (a) FSs for heavily hole-doped LaFeAsO model ($\delta n = -0.15$) for $\Delta_E = 50$meV. (b) Obtained θ dependences of $\gamma^b_{\boldsymbol{k}}$

D: Orbital polarization only on the electron FSs in the LaFeAsO model

In the main text, we employed the constant orbital polarization $\Delta E_{xz}(\boldsymbol{k}) = -\Delta_E$, $\Delta E_{yz}(\boldsymbol{k}) = \Delta_E$ in the LaFeAsO model. In order to verify the validity of the results obtained in the main text, here we introduce the orbital polarization $\Delta E_{xz}(\boldsymbol{k}) = -\Delta E_{yz}(\boldsymbol{k}) = -\Delta_E$ only around the X, Y points whereas $\Delta E_{xz}(\Gamma) = \Delta E_{yz}(\Gamma) = 0$. Such $\boldsymbol{k}$-dependent orbital polarization has been reported by the ARPES measurement in $BaFe_2As_2$ [28]. In Fig. S5(a), we show the FSs for $\Delta_E = 50$meV. For $r = 0.334$, the obtained ρ_μ and $\tilde{S}_\mu$ as functions of $\Delta E_{xz}(\mathrm{Y})$ are shown in Figs. S5(b) and S5(c), respectively. The obtained anisotropies of ρ and S are essentially similar to those in Figs. 3(a) and 4(a) in the main text.

E: Results including the effect of the SOI in FeSe

In the main text, the spin-orbit interaction (SOI) is not taken into account. Here, we study the effect of the SOI, which is expressed as $\lambda \sum_i \boldsymbol{l}_i \cdot \boldsymbol{\sigma}_i$. The matrix elements of $\boldsymbol{l}_i$ are given in Ref. [39] . In the presence of the SOI, we have to study the sixteen-orbital model in the folded Brillouin zone (BZ) picture since the "unfolding" is prohibited by the SOI. Since the numerical calculation becomes heavy in the presence of the SOI, we take smaller $N = N_x \times N_y = 64 \times 64$ $\boldsymbol{k}$ meshes and 512 Matsubara frequencies compared to the main text.

In Fig. S6(a), we show the FSs for FeSe in the folded BZ (dotted line) for the SOI $\lambda = 50$meV and

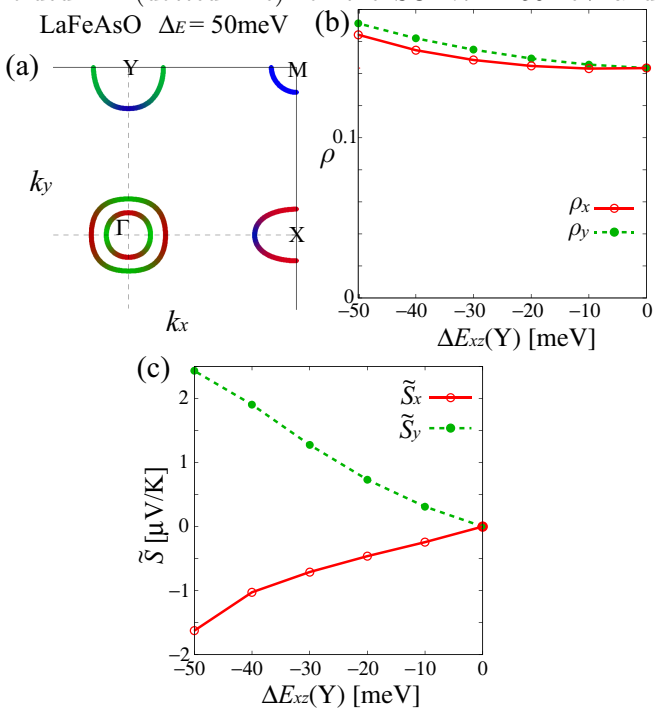

FIG. S5: (a) FSs of the LaFeAsO model for $\Delta_E = 50$meV only on the e-FSs ($\alpha_s = 0.983$). $\Delta E_{xz}(\mathrm{Y})$ dependences of (b) ρ_μ and (c) $\tilde{S}_\mu$.

$\Delta_E = 30$meV. The employed $\Delta E_{xz(yz)}(\boldsymbol{k})$ is the same as that employed in the main text. We put $r = 0.225$. In this case $\alpha_s = 0.870$ is satisfied for $\Delta_E = 50$meV. The obtained ρ_μ is shown in Figs. S6(b) as a function of $\Delta_{xy}(\mathrm{Y})$. The obtained result is qualitatively the same as the results without the SOI shown in Fig. 3 in the main text. In Fig. S6(c), we show the obtained $\tilde{S}_\mu$ as a function of $\Delta_{xy}(\mathrm{Y})$. The obtained anisotropy of S is small because of the nearly symmetric energy dependence of $1/\gamma^{b=2}_{\boldsymbol{k}}$ due to the moderate spin fluctuations in FeSe.

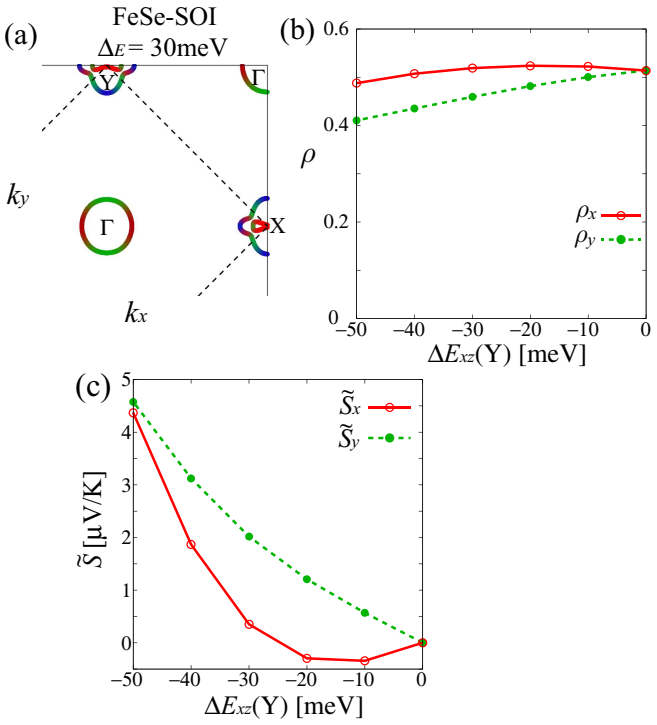

FIG. S6: (a) FSs of the 16 orbital *d-p* FeSe model for $\Delta_E = 30$meV and SOI $\lambda = 50$meV ($\alpha_s = 0.865$). ΔE_{xz}(Y) dependence of (b) ρ_μ and (c) $\tilde{S}_\mu$ for $\lambda = 50$meV.